




## Article

# Cyano/Hydroxyl Groups Co-Functionalized g-C<sub>3</sub>N<sub>4</sub> for Photocatalytic NO Removal: A Synergistic Strategy towards Inhibition of Toxic Intermediate NO<sub>2</sub>

Hui Wang <sup>1</sup>, Xiaoqian Xu <sup>1</sup>, Abdelkader Labidi <sup>1</sup>, Haitao Ren <sup>1</sup>, Ahmed A. Allam <sup>2</sup>, Ahmed Rady <sup>3</sup> , Yu Huang <sup>4,5</sup> , Shuwei Wei <sup>1</sup>, Mohsen Padervand <sup>6,\*</sup>, Shahnaz Ghasemi <sup>7</sup> and Chuanyi Wang <sup>1,\*</sup> 

- <sup>1</sup> School of Environmental Science and Engineering, Shaanxi University of Science and Technology, Xi'an 710021, China; bs200311002@sust.edu.cn (H.W.); cb200311003@sust.edu.cn (X.X.); abdelkaderlabidi0907@gmail.com (A.L.); bs210311007@sust.edu.cn (H.R.); 200311006@sust.edu.cn (S.W.)
- <sup>2</sup> Zoology Department, Faculty of Science, Beni-Suef University, Beni-Suef 62511, Egypt; ahmed.aliahmed@science.bsu.edu.eg
- <sup>3</sup> Department of Zoology, College of Science, King Saud University, P.O. Box 2455, Riyadh 11451, Saudi Arabia; ahabdo@ksu.edu.sa
- <sup>4</sup> Key Laboratory of Aerosol Chemistry and Physics, State Key Lab of Loess and Quaternary Geology (SKLLQG), Institute of Earth Environment, Chinese Academy of Sciences, Xi'an 710061, China; huangyu@ieecas.cn
- <sup>5</sup> CAS Center for Excellence in Quaternary Science and Global Change, Institute of Earth Environment, Chinese Academy of Sciences, Xi'an 710061, China
- <sup>6</sup> Department of Chemistry, Faculty of Science, University of Maragheh, Maragheh P.O. Box 55181-83111, Iran
- <sup>7</sup> Sharif Energy, Water, and Environment Institute, Sharif University of Technology, Azadi Avenue, Tehran P.O. Box 11365-8639, Iran; sh.ghasemi@sharif.ir
- \* Correspondence: padervand@maragheh.ac.ir (M.P.); wangchuanyi@sust.edu.cn (C.W.)

**Abstract:** Photocatalytic NO removal is usually accompanied by the generation of NO<sub>2</sub>, an intermediate with a higher toxicity than NO. Therefore, it is critically important to develop new photocatalysts capable of NO selective conversion. Herein, we report on the synergistic roles of cyano and hydroxyl functional groups in photocatalytic NO removal. According to the results, the NO<sub>2</sub> production efficiencies on cyano/hydroxyl-group-modified g-C<sub>3</sub>N<sub>4</sub> (DCN-O-R) was limited to 4.8%, which was lower than that of cyano-group-modified g-C<sub>3</sub>N<sub>4</sub> (DCN, 38.6%) and pure g-C<sub>3</sub>N<sub>4</sub> (CN, 50.0%). Meanwhile, the photocatalytic NO conversion efficiency over DCN-O-R was higher than that of DCN and g-C<sub>3</sub>N<sub>4</sub>. It was found that the insertion of cyano groups favorably changes the energy band of g-C<sub>3</sub>N<sub>4</sub> towards the generation of •O<sub>2</sub><sup>-</sup>. NO can only be oxidized to NO<sub>2</sub> by the photogenerated holes. When NO<sub>2</sub> is adsorbed on the surface of hydroxyl groups, it can be further oxidized to the product NO<sub>3</sub><sup>-</sup> by •O<sub>2</sub><sup>-</sup>. The synergistic effect of bifunctional groups regulates the conversion pathway from NO→NO<sub>2</sub> to NO→NO<sub>2</sub>→NO<sub>3</sub><sup>-</sup>. This work provides a strategy to abate toxic intermediates during the NO removal process, underlining the importance of surface/interface molecular engineering in regulating catalytic reaction pathways.

**Keywords:** photocatalysis; g-C<sub>3</sub>N<sub>4</sub>; cyano groups; hydroxyl groups; NO removal



**Citation:** Wang, H.; Xu, X.; Labidi, A.; Ren, H.; Allam, A.A.; Rady, A.; Huang, Y.; Wei, S.; Padervand, M.; Ghasemi, S.; et al. Cyano/Hydroxyl Groups Co-Functionalized g-C<sub>3</sub>N<sub>4</sub> for Photocatalytic NO Removal: A Synergistic Strategy towards Inhibition of Toxic Intermediate NO<sub>2</sub>. *Catalysts* **2023**, *13*, 1433. <https://doi.org/10.3390/catal13111433>

Academic Editor: Maria J. Sabater

Received: 30 September 2023

Revised: 4 November 2023

Accepted: 8 November 2023

Published: 13 November 2023



**Copyright:** © 2023 by the authors. Licensee MDPI, Basel, Switzerland. This article is an open access article distributed under the terms and conditions of the Creative Commons Attribution (CC BY) license (<https://creativecommons.org/licenses/by/4.0/>).

## 1. Introduction

The increasing number of motor vehicles and industrial activities is causing serious environmental pollution [1–3]. As a common gaseous pollutant, nitrogen oxide (NO<sub>x</sub>) can not only cause respiratory and cardiopulmonary diseases, but also produces ozone, acid rain, haze, photochemical smog, and other environmental issues. It is a serious hazard to the ecosystem and human health [4–6]. Traditional technologies, such as liquid adsorption [7], solid adsorption [8], three-way catalyst (TWC) [9], selective catalytic reduction (SCR) [10–12] and selective non-catalytic reduction (SNCR) [13], are mainly aimed at point

source pollution with high concentrations and it is difficult to remove low concentration- $\text{NO}_x$  (ppm to ppb levels). In addition, these technologies usually have the drawbacks of strict reaction conditions, high energy consumption, low efficiency, catalyst deactivation, and secondary pollution [14,15]. Compared with traditional technologies, photocatalysis, as an efficient and environmentally friendly technology, has shown great potential in solving  $\text{NO}_x$  pollution problems. The bandgap of a semiconductor is excited when the energy of a photon equals or exceeds its bandgap. In contrast to photogenerated holes ( $\text{h}^+$ ), which remain in the valence band, photogenerated electrons ( $\text{e}^-$ ) migrate from the valence band (VB) to the conduction band (CB).  $\text{e}^-$  and  $\text{h}^+$  pairs travel from the bulk of the photocatalyst to the surface and initiate subsequent redox reactions, resulting in efficient NO removal [16].

Among the photocatalytic materials, a great deal of attention has been paid to graphitic carbon nitride ( $\text{g-C}_3\text{N}_4$ ) because of its abundance as a raw material, lack of toxicity, straightforward production procedure, reactivity to visible light, outstanding chemical stability, and tunable electronic structure [17,18]. However,  $\text{g-C}_3\text{N}_4$  exhibits poor NO removal ability due to intrinsic limitations such as a small surface area, narrow absorption range for visible light, low separation and migration efficiency, and the rapid recombination of photogenerated carriers [19]. In addition, the high valence band position of  $\text{g-C}_3\text{N}_4$  restricts its oxidizing ability, resulting in the incomplete oxidation of NO [20,21]. The product contains a large amount of  $\text{NO}_2$ , which is more toxic than NO [22,23]. These obstacles limit the practical application of  $\text{g-C}_3\text{N}_4$  for photocatalytic NO removal. Further modification of  $\text{g-C}_3\text{N}_4$  is required for efficient and complete NO removal. In recent years, various strategies have been extensively studied, including morphology modulation [24], heteroatom doping [25,26], defect engineering [27], functional groups modification [28], metal loading [29,30], heterostructure building [31], etc. Among them, the modification of  $\text{g-C}_3\text{N}_4$  with suitable functional groups is considered as an effective strategy for the selective photocatalytic conversion of gaseous pollutants.

It has been reported that  $\text{g-C}_3\text{N}_4$  modified with various agents, such as cyano [32], carbonyl [33], carboxyl [34], and hydroxyl [35], indicated better performance than pristine carbon nitride due to the favorable effects of the functional groups, which not only improve the optical absorption properties but also ameliorate the adsorption capacity on the surface, thereby enhancing photocatalytic performance. However, only a few studies are concerned with the photocatalytic conversion of NO. Zeng [36] et al. prepared hydroxyl and carbonyl co-modified  $\text{g-C}_3\text{N}_4$ . The results demonstrated that the functional groups can successfully inhibit the recombination of photogenerated electron-hole pairs by modulating the band structure of  $\text{g-C}_3\text{N}_4$ . Although this work indicates an improvement in NO removal efficiency, a large number of toxic products are generated in the conversion process. These studies showed that functional groups modification could improve the photocatalytic performance of  $\text{g-C}_3\text{N}_4$ . However, the mechanistic roles of functional groups towards the selective conversion of NO to the products with less toxicity under illumination are rarely studied and still unclear. There are some scientific issues that merit further study.

Based on the above considerations, we successfully prepared novel cyano/hydroxyl/ $\text{g-C}_3\text{N}_4$  materials using a simple pyrolysis method. Making use of several characterization techniques, the effects of surface functionalization on modulating the structural and electronic features of graphitic carbon nitride are described in details. The product evolution process of NO conversion over cyano- and hydroxyl-group-modified  $\text{g-C}_3\text{N}_4$  (DCN-O-R) photocatalyst was dynamically monitored by in situ DRIFTS. The scavenging experiment and ESR were also used to reveal the key reactive oxygen species (ROS) in the process of NO selective conversion. The prominent roles of the aforementioned functional groups in regulating the morphological properties at the molecular level and inhibiting the charge carriers' recombination to direct the mechanism of the photoreaction are comprehensively discussed. Our findings demonstrate that the co-functionalization of  $-\text{C}\equiv\text{N}$  and  $-\text{OH}$  on  $\text{g-C}_3\text{N}_4$  significantly promotes the complete oxidation of NO to the product  $\text{NO}_3^-$  through

a two-step reaction ( $\text{NO} \rightarrow \text{NO}_2 \rightarrow \text{NO}_3^-$ ) and inhibits the formation of toxic  $\text{NO}_2$ , which is of great importance in practical applications.

## 2. Results and Discussion

The synthesis process of DCN and DCN- $x$  is shown in Figure 1. The first calcination can form DCN. After the second calcination, under different conditions, DCN-O- $x$  will be formed. The crystalline phases of the as-prepared samples are demonstrated using the XRD patterns. As can be seen in Figure 2a, all samples have the two classic  $g\text{-C}_3\text{N}_4$  diffraction peaks at  $13.0^\circ$  and  $27.8^\circ$ , which are attributed to the (110) and (002) crystal planes, representing the in-plane repeating units and the stacking reflection of the inter-layer, respectively [37]. The two characteristic peaks of DCN and DCN- $x$  become weaker as compared to CN, reflecting the loss of long-range planned structures within the  $g\text{-C}_3\text{N}_4$  framework. This result may be due to the addition of  $\text{NH}_4\text{Cl}$ , which acts as a bubble template to disrupt the hydrogen bonds between the layers and insert defects in the heptazine, leading to the destruction of the in-plane repeating units [38]. As shown in Figure 2b, the characteristic peak of DCN and DCN-O- $x$  (002) plane shift from  $27.2^\circ$  to  $27.4^\circ$  compared to CN, which reflects the decrease in the stacking distance between the layers [39]. This observation can be assigned to the presence of structural defects in the  $g\text{-C}_3\text{N}_4$  framework [40].

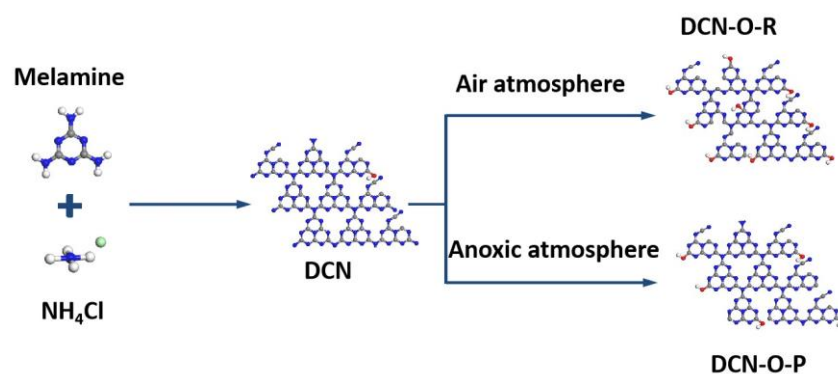


**Figure 1.** The synthesis process of cyano-group-modified  $g\text{-C}_3\text{N}_4$  (DCN) and  $g\text{-C}_3\text{N}_4$  modified with cyano/hydroxyl groups of different hydroxyl concentrations (DCN- $x$ ).

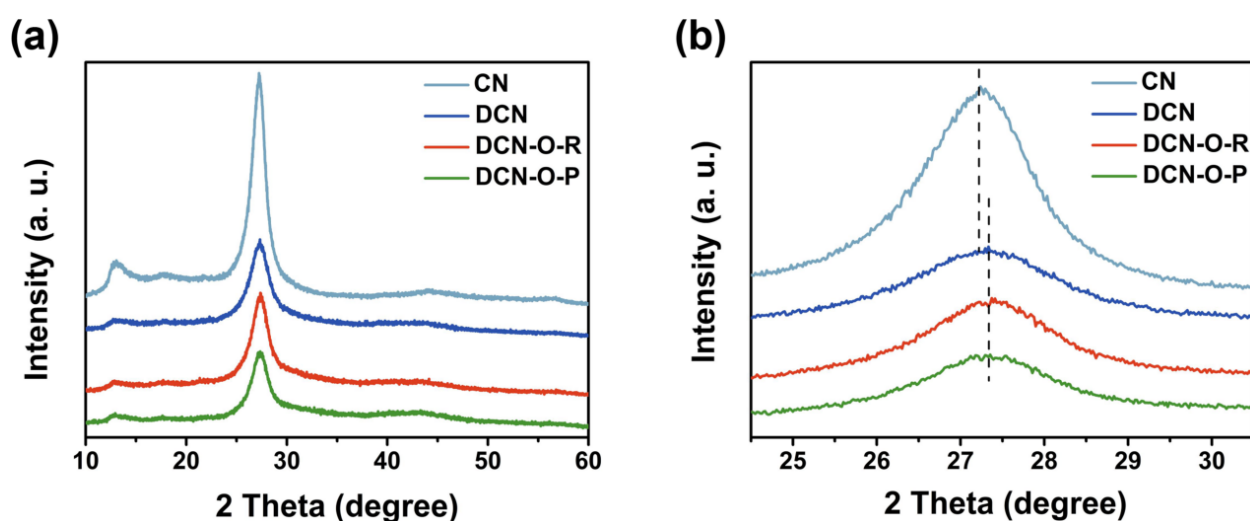


**Figure 2.** (a) XRD patterns; and (b) enlarged XRD patterns of  $g\text{-C}_3\text{N}_4$  (CN), DCN and DCN- $x$  samples.

The morphology of DCN-O-R was investigated by transmission electron microscopy (TEM). As shown in Figure 3a,b, DCN-O-R shows a porous framework. The position

marked by the red circle can clearly observe the porous framework. In fact, ammonium chloride decomposes into gas at 337 °C [41], which provides abundant bubble templates during calcination. The specific surface area and pore size can both be increased by secondary calcination. The specific surface area and porosity of the structures remarkably influence the adsorption capacity and the number of catalytic active sites [42].

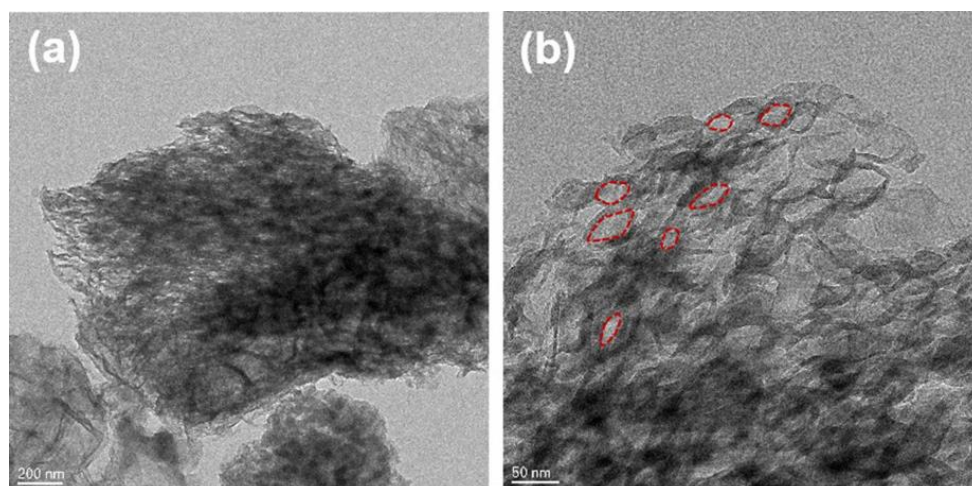


**Figure 3.** TEM images of cyano/hydroxyl-group-modified  $g\text{-C}_3\text{N}_4$  (DCN-O-R) (a,b) at different magnifications.

To further evaluate the porosity and specific surface area,  $\text{N}_2$  adsorption-desorption isotherms were used to describe the pore shape and size distribution. From Figure A2a, all samples exhibit type IV isotherms with H3 hysteresis loops [43]. The specific surface area of DCN prepared by adding  $\text{NH}_4\text{Cl}$  is  $42.95 \text{ m}^2 \cdot \text{g}^{-1}$ , is much higher than that of CN ( $3.70 \text{ m}^2 \cdot \text{g}^{-1}$ ). The specific surface areas of DCN-O-R and  $g\text{-C}_3\text{N}_4$ , containing cyanide and a small amount of hydroxyl groups prepared under hypoxic conditions (DCN-O-P), are significantly increased to  $75.07$  and  $63.08 \text{ m}^2 \cdot \text{g}^{-1}$ , respectively. As shown in Figure A2b, the Barret-Joyner-Halenda (BJH) analysis shows that the maximum distribution of DCN pore sizes is around 20–40 nm. After secondary calcination, the pores of DCN-x are more abundant than that of DCN, which is consistent with the TEM image results. The size of the pores has also increased at the same time. The pore diameters of DCN-O-R and DCN-O-P range from 30 to 50 nm. The results well demonstrate that  $\text{NH}_4\text{Cl}$ -assisted heat treatment and secondary calcination increase the  $g\text{-C}_3\text{N}_4$  specific surface area and form the porous structure. In this way, there are more reactive sites on the surface of the photocatalyst.

The chemical structure and composition of the samples were examined using FT-IR and XPS analysis methods. FT-IR spectra can provide useful structural information about the chemical bonds in the samples. All the materials show similar FT-IR patterns, as illustrated in Figure 4a. The formation of triazine-based  $\text{C}_3\text{N}_4$  can be excluded, as evidenced by the absence of its characteristic band at  $995 \text{ cm}^{-1}$ . The strong peaks in the range of  $1700\text{--}1200 \text{ cm}^{-1}$  are attributed to the typical stretching vibrations of the heptazine ring. The peak at  $807 \text{ cm}^{-1}$  is attributed to the typical bending vibration of the heptazine ring [44]. The stretching vibration of the N-H bond can be explained by the broad peaks in the  $3650\text{--}3000 \text{ cm}^{-1}$  region [45]. The results indicate that all samples have an ordered planar structure composed of heptazine units. However, compared with CN, DCN and DCN-x display a novel vibrational band at  $2178 \text{ cm}^{-1}$ , which is attributed to  $\text{-C}\equiv\text{N}$  groups [46]. As shown in Figure 4b, the DCN-x samples display a novel peak at  $1280 \text{ cm}^{-1}$ , which can be attributed to the  $\text{-OH}$  groups [38]. The above results demonstrate that DCN-O-R is co-modified by cyano and hydroxyl functional groups. Accordingly, the  $\text{NH}_4\text{Cl}$ -assisted heat treatment can insert  $\text{-C}\equiv\text{N}$  group into the DCN structure, while the secondary calcination effectively inserts the  $\text{-OH}$  group into DCN-x.

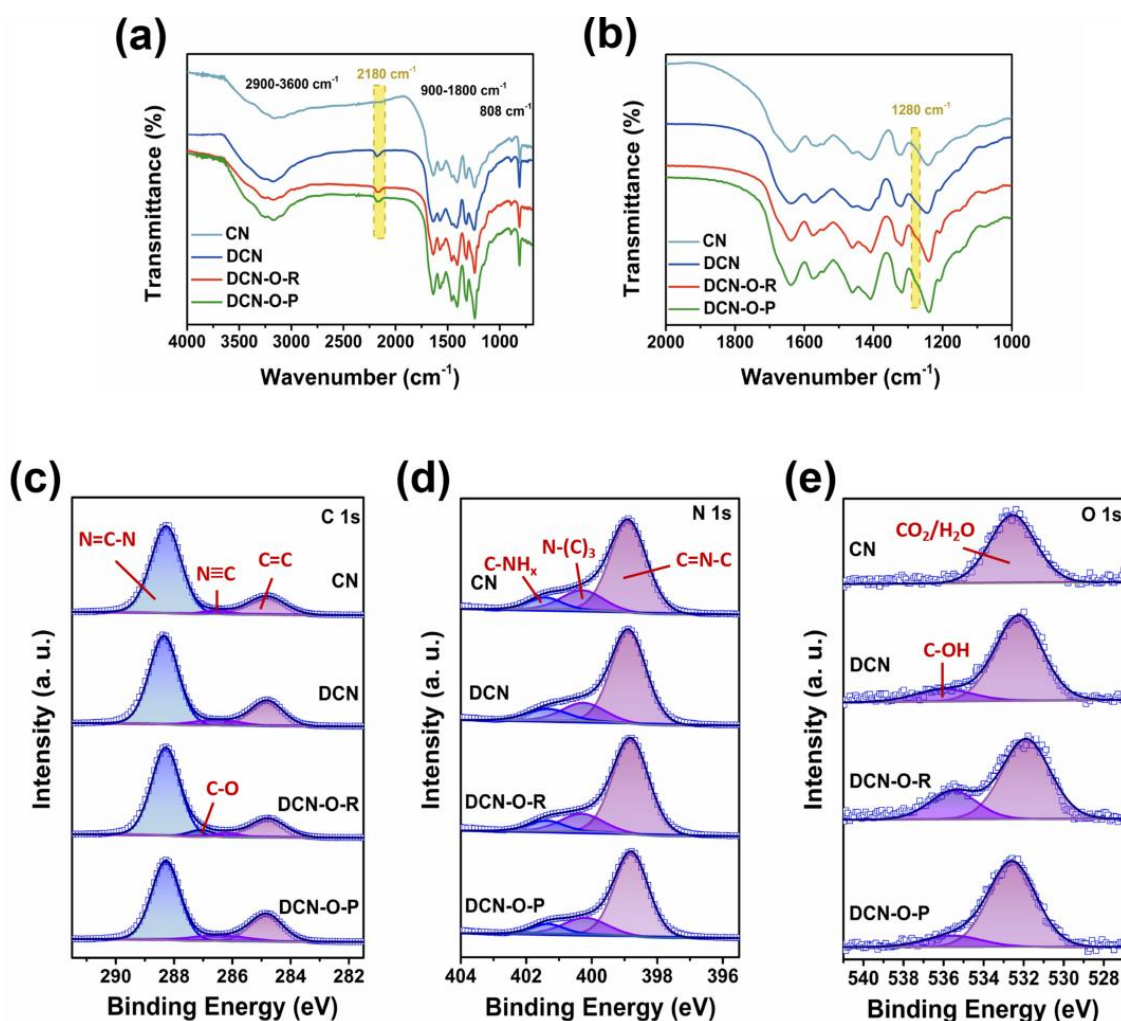


**Figure 4.** (a) FT-IR spectra; (b) enlarged FT-IR spectra in the range of 1000 to 2000  $\text{cm}^{-1}$ ; high-resolution XPS spectra of (c) C 1s; (d) N 1s; and (e) O 1s of CN, DCN and DCN-x samples.

To further confirm the effect of the  $\text{NH}_4\text{Cl}$  heat treatment and secondary calcination under different atmospheric conditions on the structure of  $\text{g-C}_3\text{N}_4$ , all samples were characterized by X-ray photoelectron spectroscopy (XPS). As shown in Figure A3, the XPS survey scan spectra show that all samples contain carbon, nitrogen, and a small amount of oxygen. The ratios of N-to-C and O-to-C of all samples are shown in Table A1. During the preparation process, some defects may form, such as nitrogen vacancies, resulting in a ratio lower than the ideal ratio of 1.33. In addition, the second calcination will increase the concentration of nitrogen vacancies and introduce the hydroxyl groups. When nitrogen atoms are lost, the N-to-C ratio will decrease. As the hydroxyl group increases, the O-to-C ratio also increases. Figure 4c–e depicts high-resolution XPS spectra of C 1s, N 1s, and O 1s. The N 1s high-resolution spectra of CN, DCN and DCN-x can be fitted into three peaks at the binding energies of 398.6, 400.1, and 401.2 eV (Figure 4d), which are assigned to N-C, N-(C)<sub>3</sub>, and C-NH<sub>x</sub>, respectively. The intensity of the peak at the 401.2 eV binding energy is not significantly enhanced, indicating no significant increase in the number of -NH<sub>x</sub> groups. The C 1s high-resolution spectra of CN, DCN and DCN-x, as shown in Figure 4c, can be fitted into three peaks at binding energies of 284.8, 286.37, and 288.3 eV, which are assigned to N-C=N, C-NH<sub>x</sub>, or C≡N [47], and  $sp^2$ -hybridized carbon, respectively [48]. Compared to CN, the intensities of the characteristic peaks of DCN and DCN-x located at the binding energy of 286.37 eV increased, indicating that DCN and DCN-x contain high concentrations of the -C≡N group. It is worth noting that, except for the above three peaks, a new peak at the binding energy of 284.1 eV is displayed in the C 1s spectrum of DCN-O-R.

This peak is attributed to C–OH, which confirms the existence of –OH groups through the binding to C [49]. Figure 4e demonstrates that a peak at binding energy 532.8 eV can be observed in the O 1s high-resolution spectrum of CN. This peak is considered to be caused by CO<sub>2</sub> or H<sub>2</sub>O absorbed on the sample's surface [50,51]. A novel peak at the binding energy of 535.5 eV can be observed in the O 1s fitting spectra of DCN and DCN–x, which is due to the existence of –OH groups on the sample [51]. This result is consistent with the FT–IR spectra. The intensities of these peaks of DCN–x are much higher than those of DCN, indicating that the –OH group can be effectively introduced into the surface of DCN–x by secondary calcination. The concentrations of the –OH group in DCN–x are different under different atmospheric conditions. Among them, the concentrations of the –OH group on the DCN–O–R surface are the highest.

Room-temperature electron paramagnetic resonance (EPR) spectroscopy was used to analyze the changes in the electronic properties of the photocatalysts. The absence of nitrogen atoms leads to the presence of nitrogen vacancies in the g-C<sub>3</sub>N<sub>4</sub> structure. After the N atom is lost, there are no paired electrons on the C atom, and the EPR signal will be enhanced. As shown in Figure 5, a single Lorentzian signal of  $g = 2.0046$  can be observed in all samples due to the unpaired electrons in the heptazine ring of g-C<sub>3</sub>N<sub>4</sub> [52]. The signal intensity in the DCN's pattern is higher than that of CN, which proves that nitrogen vacancies are introduced into DCN during the NH<sub>4</sub>Cl-assisted heat treatment steps [53]. Obviously, secondary calcination of DCN can increase the nitrogen vacancy concentration significantly. Similar amounts of nitrogen vacancies exist in both DCN–O–R and DCN–O–P samples.

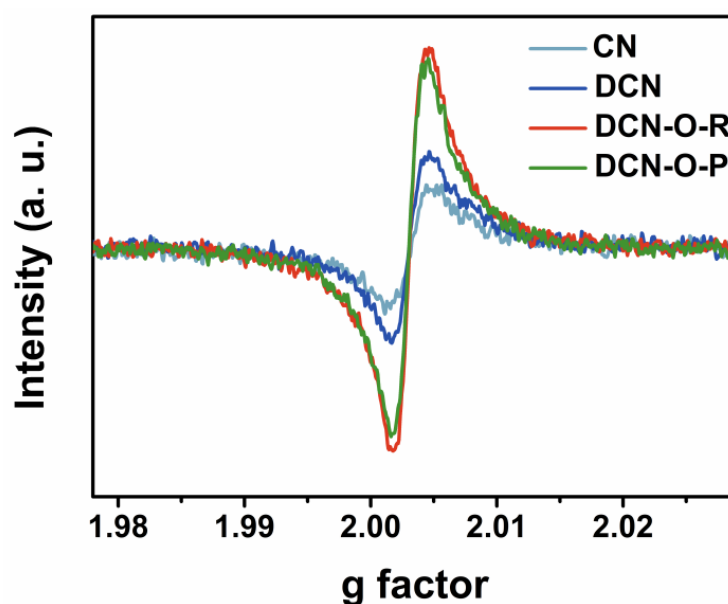
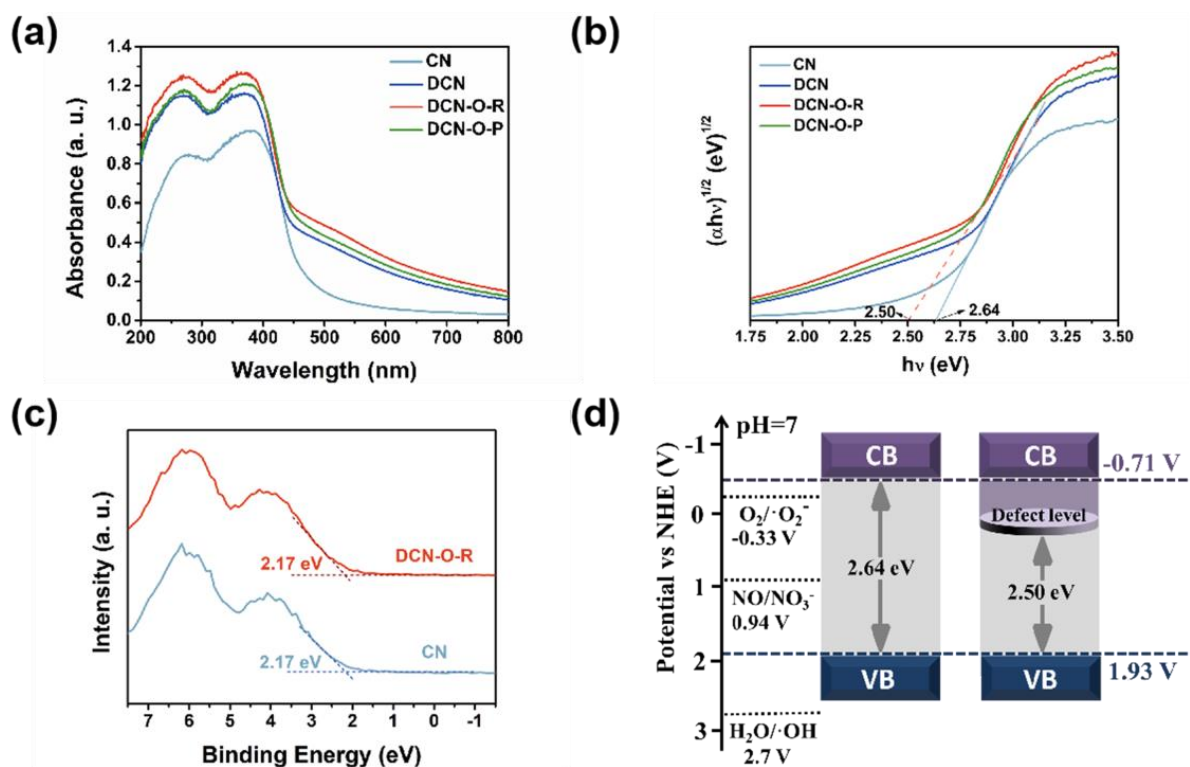


Figure 5. EPR spectra of CN, DCN and DCN–x samples.

Light-harvesting features and bandgap values, in particular, are of great significance in photocatalytic processes. UV–Vis diffuse reflectance spectroscopy (UV–Vis DRS) and XPS valence band spectra were used to analyze the effects of nitrogen vacancies, –C≡N, and –OH groups on the band structure and optical properties of the samples. As shown in Figure 6a, all samples are able to absorb the photons in the visible light region. However, compared with CN, DCN and DCN–x have increased optical absorption ability and show a significant redshift of the optical absorption edge. In addition, the absorption tails of DCN and DCN–x in the range of 450–600 nm have obvious surges, suggesting that the samples have a bandgap [41]. Structural defects, impurities, and other surface adsorbents can lead to electron localization. Therefore, the localized electrons in DCN and DCN–x may be caused by cyanide groups, resulting in absorption tails in the range of 450–600 nm.

The absorption tails of DCN and DCN-*x* are similar, demonstrating that the insertion of the bandgap is mostly influenced by  $-\text{C}\equiv\text{N}$  groups and only slightly affected by the  $-\text{OH}$  groups, but not affected by nitrogen vacancies. The results demonstrate that modification of  $g\text{-C}_3\text{N}_4$  with  $-\text{C}\equiv\text{N}$  groups can further expand photocatalytic performance to the visible light region.



**Figure 6.** (a) UV-Vis DRS; (b) plots of  $(\alpha h\nu)^{1/2}$  versus  $(h\nu)$ ; (c) XPS valence band spectra; and (d) electronic band structure of CN and DCN-*x* samples.

The bandgap energy ( $E_g$ ) of the samples was estimated by the Tauc formula,  $(\alpha h\nu) = A(h\nu - E_g)^{1/2}$  [54]. As shown in Figure 6b, the intrinsic bandgap of both CN and DCN-O-R is 2.64 eV. Notably, the bandgap energy of DCN-O-R is 2.50 eV. A narrow bandgap is favored to harvest light photons efficiently and promote photogenerated electron transport [55]. In addition, the XPS valence band spectra were utilized to investigate the valence band positions of the samples. As exhibited in Figure 6c, the VB edge positions of CN and DCN-O-R are both 2.17 eV. The following equation can be used to eliminate the measurement error:

$$\text{VB (vs. NHE)} = \Phi + \text{VB}_{\text{XPS}} - 4.44 \text{ eV}$$

where  $\Phi$  (4.2 eV) corresponds to the XPS analyzer's work function, and 4.44 eV is obtained from the vacuum level [56]. The VB positions (relative to NHE) of CN and DCN-O-R are both 1.93 V. From these results, and, combined with the obtained bandgaps, Figure 6d shows the detailed band structures of CN and DCN-O-R. According to calculations, the conduction band edges of CN and DCN-O-R are located at  $-0.71$  V. The new defect state formed below the conduction band of DCN-O-R acts as an intermediate energy level and its position is calculated to be  $-0.57$  V. This potential still enables the easy conversion of  $\text{O}_2$  to superoxide radicals ( $\bullet\text{O}_2^-$ ), which is favored thermodynamically ( $\text{O}_2/\bullet\text{O}_2^- = -0.33$  V) [27].

Photocatalytic NO removal performance was evaluated using a continuous flow reactor. The samples were placed in the dark until NO adsorption reached an equilibrium. The samples' photocatalytic activities were then evaluated under visible light ( $\lambda > 420$  nm). Figure 7a shows the NO removal efficiencies ( $1 - C/C_0$ ) of all samples with the irradiation time. The NO removal efficiency was 23.0% after irradiating the CN sample for 15 min.

However, the removal efficiency drastically increased to 41.6, 46.2, and 41.2% over DCN, DCN-O-R, and DCN-O-P, respectively, within the same period of reaction time. Obviously, DCN and DCN-x samples can remove NO more efficiently than CN. Among them, DCN-O-R has the best photocatalytic performance, and its photocatalytic NO removal activity is twice that of CN's activity. Notably, the removal efficiency of DCN and DCN-x are slightly different, implying that the  $-C\equiv N$  groups are the remarkable factor for the enhanced charge separation and transfer, which can significantly improve the photocatalytic performance of  $g-C_3N_4$ .

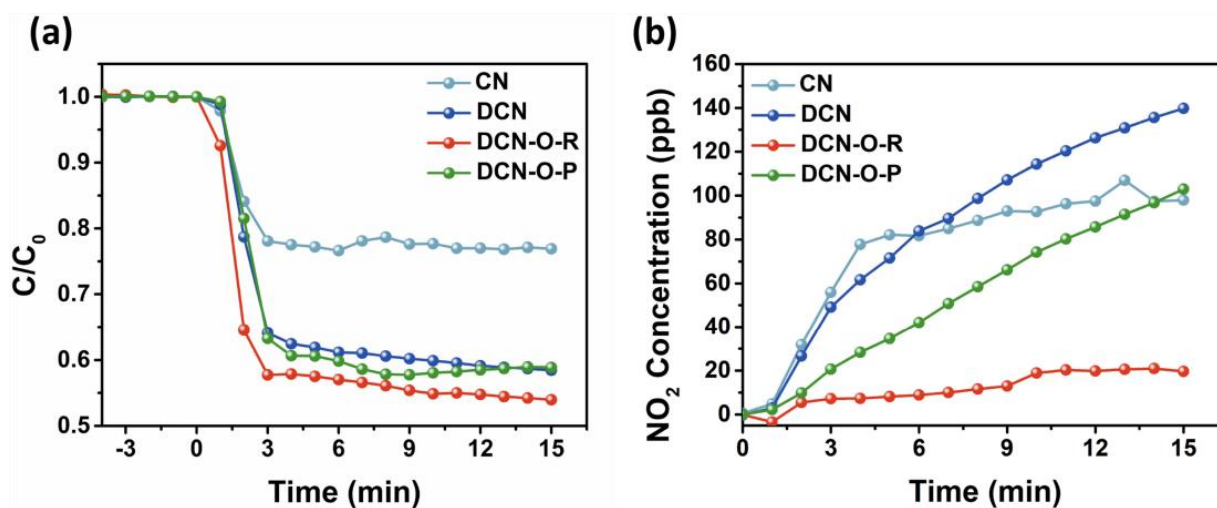


**Figure 7.** (a) Photocatalytic NO removal efficiency; and (b) the variation of  $NO_2$  yields over the prepared photocatalysts.

In addition to following the NO concentration during the photocatalytic process, the  $NO_2$  concentration was also surveyed (Figure 7b). For CN, the  $NO_2$  concentration gradually increased with time. The  $NO_2$  concentration and conversion efficiency in the aforementioned photocatalytic system was  $\sim 98$  ppb and 49%, respectively, after 15 min of irradiation time. Obviously,  $NO_2$  is a significant byproduct of the photocatalytic conversion of NO over the CN sample. The concentration of  $NO_2$  generated over DCN was approximately 140 ppb within a removal efficiency of 39%. After secondary calcination at different atmospheric conditions, DCN-O-R and DCN-O-P produced 19 and 103 ppb of  $NO_2$  concentrations, respectively, in the system, where the removal efficiency decreased to 4.8 and 31%, respectively. From the abovementioned photocatalytic results and structural information, it can be claimed that the concentration of  $-C\equiv N$  functional groups in the DCN and DCN-x samples are quite similar. Also, DCN-O-R and DCN-O-P possess similar amounts of nitrogen vacancies, which are substantially greater than that of DCN. The concentrations of hydroxyl functional groups in the three samples differ significantly. Meanwhile, the photocatalytic NO removal activity of DCN and DCN-x are close together, while the amounts of  $NO_2$  generated over the aforementioned samples are quite different. This shows that the  $-C\equiv N$  groups are the main factor for the improvement of photocatalytic NO removal activity, while they do not play a major role in the enhancement of further reactions to  $NO_3^-$ . Moreover, the NO conversion rate and  $NO_2$  generation were not necessarily controlled by the change in nitrogen vacancy concentrations in the photocatalytic structures. Interestingly, the  $-OH$  group concentrations of the samples favorably affected the  $NO_2$  generation rate during the photocatalytic NO removal. As a key point in our findings,  $-OH$  should be co-functionalized with the cyano groups on the graphitic carbon nitride nanosheets to efficiently inhibit the generation of  $NO_2$ .

In order to find a logical explanation for the  $NO_2$  inhibition over DCN-O-R during the photocatalytic NO conversion, it is helpful to explore the types of ROS produced in various photocatalytic systems. The effect of cyano and hydroxyl groups on changing the



reaction yield and selectivity can be appropriately discussed based on the types of available ROS. First, the generation of  $\text{H}_2\text{O}_2$  in the presence of different samples was scanned by a fluorophotometer. As shown in Figure 8a–c, the signals related to  $\text{H}_2\text{O}_2$  in all samples gradually increases with the irradiation time. The production of  $\text{H}_2\text{O}_2$  in the DCN system is higher than that of DCN-O-R, but much higher than that of CN. The other types of ROS in our systems were explored by DMPO- and TEMPO-assisted ESR. As shown in Figure 8d, the peaks with intensities of 1:1:1:1 are attributed to DMPO- $\bullet\text{O}_2^-$ . The weak DMPO- $\bullet\text{O}_2^-$  signal was detected in the CN system. In the DCN and DCN-O-R systems, the intensity of the signals significantly increases, implying that a large number of  $\bullet\text{O}_2^-$  radicals are injected into the photocatalytic reaction. The signals detected in the DCN system are slightly stronger than that of the DCN-O-R. As shown in Figure 8e, there is no signal for  $\bullet\text{OH}$  in the CN, DCN and DCN-O-R systems during the photocatalytic reaction. Since the valence band positions of the samples (1.93 V vs. NHE, pH = 7) are more negative than the standard redox potential of  $\text{H}_2\text{O}/\bullet\text{OH}$  (2.7 V vs. NHE, pH = 7), the  $\bullet\text{OH}$  radicals cannot be generated in the systems. The TEMPO-assisted ESR technique was employed to detect singlet oxygen ( $^1\text{O}_2$ ). As shown in Figure 8f, the peaks with intensities of 1:1:1 in our systems under dark conditions are attributed to TEMPO- $^1\text{O}_2$ . This signal in the CN system is much stronger than that observed for the DCN and DCN-O-R, and there is no change after illumination. This shows that  $^1\text{O}_2$  cannot be produced in the photocatalytic process over CN. The signals of the DCN and DCN-O-R disappeared after illumination, which may be due to the quenching of  $^1\text{O}_2$  in the systems. Photoluminescence (PL) was used to evaluate the recombination efficiency of the photogenerated electron-hole pairs. As shown in Figure 8g, compared with CN, the emission peaks appearing at  $\sim 470$  nm for both DCN and DCN-O-R have low intensities and are quite similar, indicating that the recombination efficiency of photogenerated electron-hole pairs is lower. Also, the results imply that the insertion of  $-\text{C}\equiv\text{N}$  groups not only improves the separation efficiency of the charge carriers, but also promotes the generation of  $\text{H}_2\text{O}_2$ , leading to the generation of a high amount of ROS ( $\bullet\text{O}_2^-$ ) over the DCN and DCN-O-R. However, no new ROS species were produced by adding the  $-\text{OH}$  functional groups into the DCN-O-R. Compared with DCN, the yields of ROS over the DCN-O-R system decreased slightly, which can be attributed to the destruction of a small amount of cyano groups in the secondary calcination process. The above statements imply that the no new ROS species play a role during the NO deep oxidation over the  $-\text{OH}$  group-contained photocatalyst, which is a key point in clarifying the mechanism.

Scavenger experiments were carried out to examine the ROS and their contribution to the photocatalytic pathway. Potassium iodide (KI), potassium dichromate ( $\text{K}_2\text{Cr}_2\text{O}_7$ ), *p*-benzoquinone (PBQ), isopropanol (IPA) and histidine (HIS) were used to scavenge  $\text{h}^+$ ,  $\text{e}^-$ ,  $\bullet\text{O}_2^-$ ,  $\bullet\text{OH}$ , and  $^1\text{O}_2$  radicals, respectively. Figure 8h shows the NO removal efficiency and  $\text{NO}_2$  production yield of DCN-O-R in the presence of different scavengers. From the results, the NO removal efficiency and  $\text{NO}_2$  production rate in the presence of IPA and HIS were similar to that of the control sample, indicating that the conversion of NO is not affected by  $\bullet\text{OH}$  and  $^1\text{O}_2$ . These results are consistent with findings from the DMPO- and TEMPO-assisted ESR. The presence of PBQ, KI and  $\text{K}_2\text{Cr}_2\text{O}_7$ , however, influence photocatalytic NO removal performance significantly, implying that  $\text{h}^+$  plays a major role, and that  $\text{e}^-$  and  $\bullet\text{O}_2^-$  play secondary roles in NO removal over DCN-O-R. Among them,  $\text{e}^-$  is the root cause of  $\bullet\text{O}_2^-$  generation. As the photogenerated electrons are captured,  $\bullet\text{O}_2^-$  cannot be generated. On the other hand, more additional  $\text{h}^+$  species are available to promote the photocatalytic process effectively. Therefore, it can be expected that the photocatalytic activity is higher when capturing  $\text{e}^-$  compared to that of  $\bullet\text{O}_2^-$  direct capture. Interestingly, it can be observed that the  $\text{NO}_2$  generation rate intensifies significantly when capturing both  $\text{e}^-$  and  $\bullet\text{O}_2^-$ , indicating that  $\bullet\text{O}_2^-$  is the main ROS to inhibit  $\text{NO}_2$  generation. Notably, although DCN was able to generate a similar amount of  $\bullet\text{O}_2^-$  in the reaction system, the  $\text{NO}_2$  generation efficiency was still high. All the above results illustrate that when  $\bullet\text{O}_2^-$

exists in the photoreaction system, the  $-OH$  functional groups on the surface of carbon nitride can promote the deep oxidation of  $NO_2$  to  $NO_3^-$ .

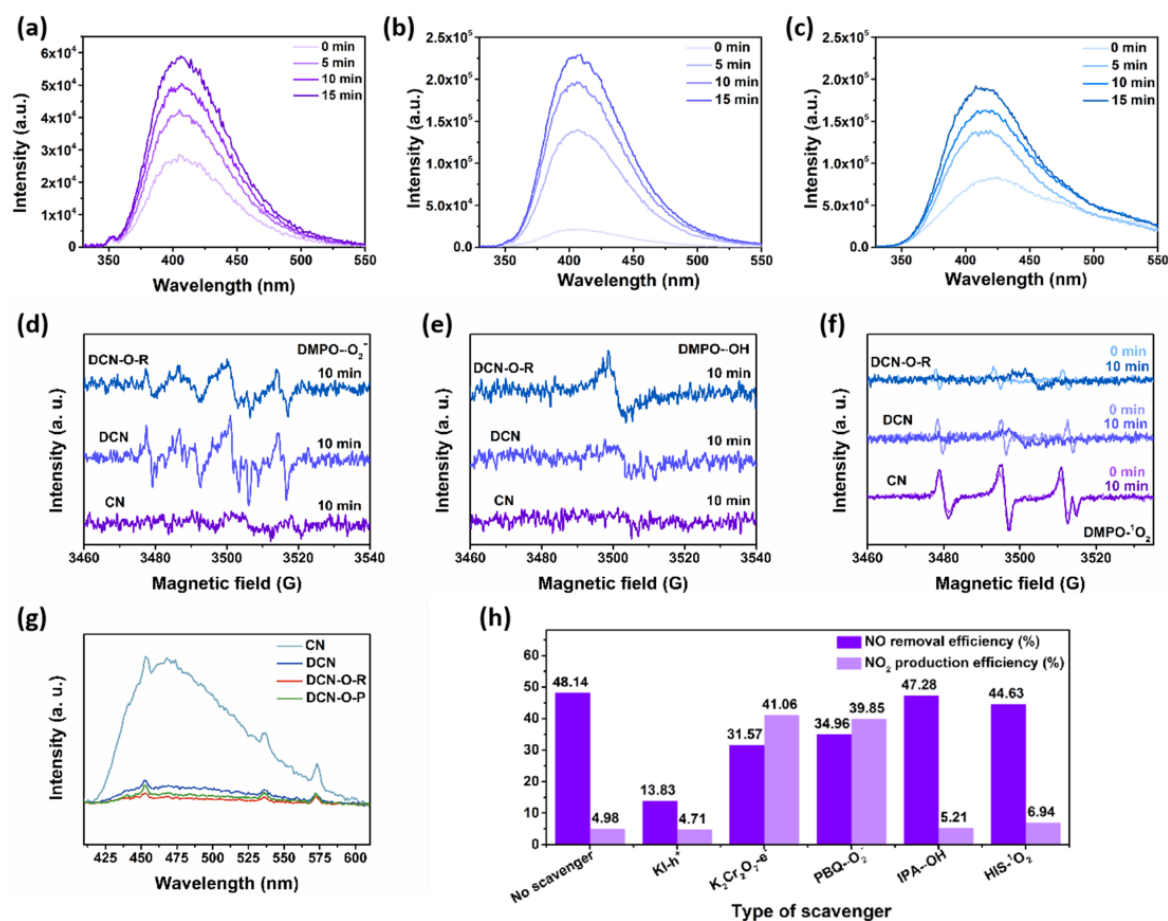


**Figure 8.** The generation of the  $H_2O_2$  in: (a) CN; (b) DCN; (c) DCN-O-R system; (d) DMPO spin-trapping ESR for  $\bullet O_2^-$  detection; (e) DMPO spin-trapping ESR for  $\bullet OH$  detection; (f) TEMPO spin-trapping ESR for  $^1O_2$  detection; (g) PL spectra of CN, DCN and DCN-O-R; and (h) the capture experiments for photocatalytic NO removal over DCN-O-R.

In situ DRIFTS was used to dynamically survey the evolution of intermediates and final products on the surface of the photocatalysts. In this way, the mechanistic effects of functional groups on the adsorption and activation of NO on the surface can be fully clarified, revealing the detailed conversion pathway of photocatalytic NO removal. The background spectra of the photocatalysts (CN and DCN-O-R) were recorded as the baselines. NO and  $O_2$  were introduced and the “in situ” DRIFTS spectra for dark adsorption were recorded within 30 min. As shown in Figure 9a, NO is physically adsorbed on CN, so that the absorption band of NO was observed at  $1085\text{ cm}^{-1}$  [57]. After NO chemisorption on the CN’s surface, *cis*- $N_2O_2$  and *trans*- $N_2O_2$  are considered to be formed, explaining the obvious absorption bands at  $1045\text{ cm}^{-1}$  and  $1016\text{ cm}^{-1}$ , respectively. The absorption peak at  $1063\text{ cm}^{-1}$  belongs to  $N_2O_2^{2-}$  [58]. In addition, the pyridine N atoms donate lone pair electrons to the  $O_2$  molecules to produce  $\bullet O_2^-$  radicals, which can oxidize  $N_2O_2$  to  $NO_2$ . The appearance of an absorption band at  $896\text{ cm}^{-1}$  can be assigned to the adsorption of  $NO_2$  in the form of  $N_2O_4$  on the surface of CN [21]. The NO adsorption pattern of DCN-O-R is quite different from that of CN. According to Figure 9c, the physical adsorption of NO on DCN-O-R can be illustrated based on the absorption band at  $1085\text{ cm}^{-1}$  [21]. The sharp band at  $1193\text{ cm}^{-1}$  describes the nitrite generated following the NO chemisorption on the DCN-O-R surface [59]. Meanwhile, the absorption band of  $NO_2^-$  can be observed at  $891\text{ cm}^{-1}$  [60]. The obtained results show that the NO oxidation reaction can proceed

slowly in the absence of illumination. In addition, an obvious absorption band is observed at  $2131\text{ cm}^{-1}$ , which is related to the adsorbed intermediate species  $-\text{C}\equiv\text{N}-\text{NO}$ .

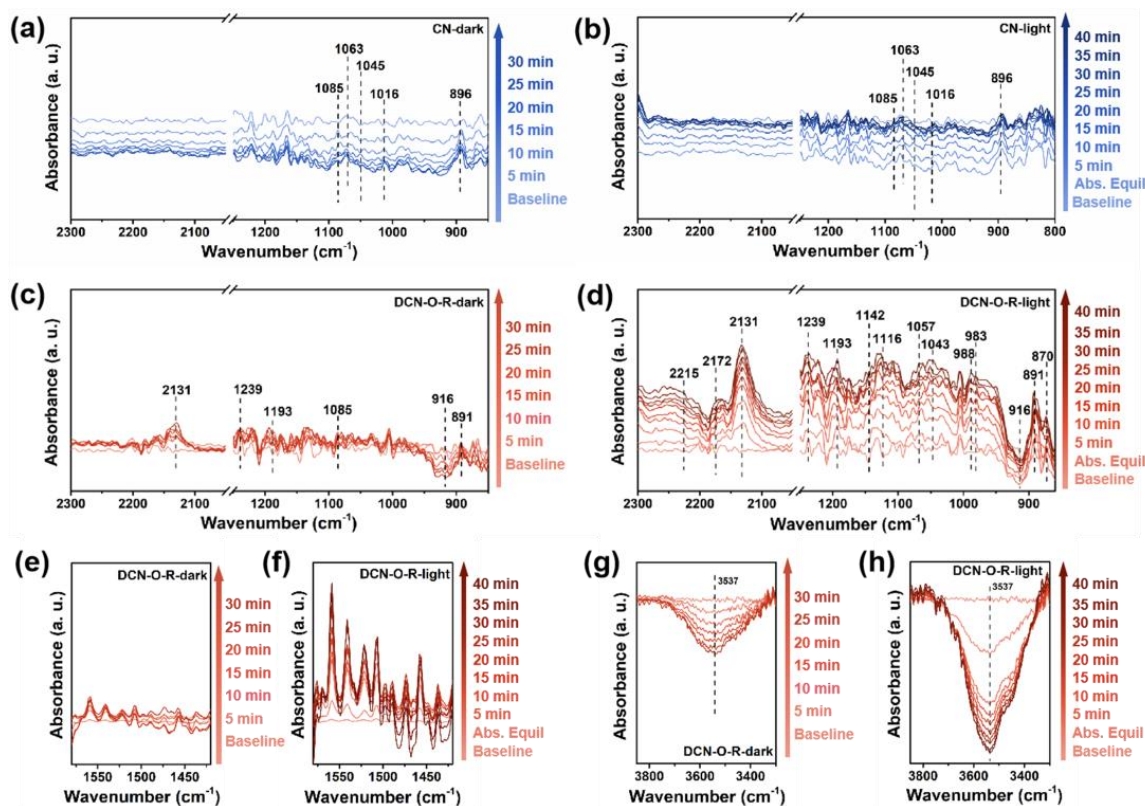


**Figure 9.** In situ DRIFTS spectra of NO adsorption (a,c, for CN and DCN-O-R, respectively) and visible light photocatalytic process (b,d, for CN and DCN-O-R, respectively). (e,f) absorption bands and (g,h) negative bands

In situ DRIFTS was also used to monitor the photocatalytic NO conversion process on CN and DCN-O-R under visible light irradiation. The photocatalytic NO conversion on CN is shown in Figure 9b. The intensities of all peaks are reduced as compared to the dark adsorption procedure, demonstrating that the intermediates adsorbed on the CN surface tended to be oxidized to  $\text{NO}_2$  by  $h^+$  during the photocatalytic process. However, the absorption peaks of DCN-O-R are different from those of CN. In situ DRIFTS spectra of the photocatalytic conversion products of NO on DCN-O-R are shown in Figure 9d. The stretching vibration of monodentate nitrite or chelated nitrite is thought to be the reason for the appearance of the peak at  $870\text{ cm}^{-1}$  [57]. The new peaks at 983, 988, 1043, 1057, and  $1116\text{ cm}^{-1}$  are correlated to the stretching vibration of chelated bidentate nitrate, monodentate nitrate, and bridging nitrate [21,55,58]. As shown in Figure 9e,f, the absorption band at  $1580\text{--}1420\text{ cm}^{-1}$  is attributed to nitrate. The peak present at  $1239\text{ cm}^{-1}$  is attributed to  $\text{N}_2\text{O}_5$  [58], and  $\text{N}_2\text{O}$  is responsible for the new peak at  $2172\text{ cm}^{-1}$  [21]. Meanwhile, the new peak observed at  $1142\text{ cm}^{-1}$  is due to  $\text{NO}^-/\text{NOH}$  [61]. The peak intensity at  $2131\text{ cm}^{-1}$  increased significantly with time, indicating that the adsorption and activation of NO molecules on  $-\text{C}\equiv\text{N}$  groups of DCN-O-R are significantly improved. Additionally, we found another extra peak at  $2215\text{ cm}^{-1}$  which could correspond to the  $\text{NO}^+$  free ions formed by the oxidation of adsorbed NO by photogenerated  $h^+$  on the surface [61]. As shown in Figure 9g,h, the negative band at  $3500\text{ cm}^{-1}$  is attributed to the negative peak of the  $-\text{OH}$  stretching vibration, which may be due to the loss of the H atoms of hydroxyl groups. The negative band present at  $916\text{ cm}^{-1}$  is attributed to the loss of the H atoms of the hydroxyl group [62].

Based on the results of trapping experiments and in situ DRIFTS, a plausible mechanism can be proposed, as indicated in Figure 10. For the photocatalytic NO removal over DCN-O-R, both the N atoms of NO and the C atoms of  $-C\equiv N$  groups contain an unpaired electron, which can form a C–NO chemical bond through coupling [59]. However, the photogenerated electron–hole pairs are produced as DCN-O-R’s surface absorbs the visible light photons.  $e^-$  and  $h^+$  migrate from the bulk to the surface. The  $-C\equiv N$  groups can promote the conversion of  $O_2$  adsorbed on the DCN-O-R surface with  $e^-$  to form  $\bullet O_2^-$ . Meanwhile, the NO adsorbed on the  $-C\equiv N$  groups are further oxidized to  $NO_2$  by  $h^+$ . Subsequently,  $NO_2$  can adsorb on the  $-OH$  groups of DCN-O-R and be further oxidized by  $\bullet O_2^-$  to form the final product ( $NO_3^-$ ).

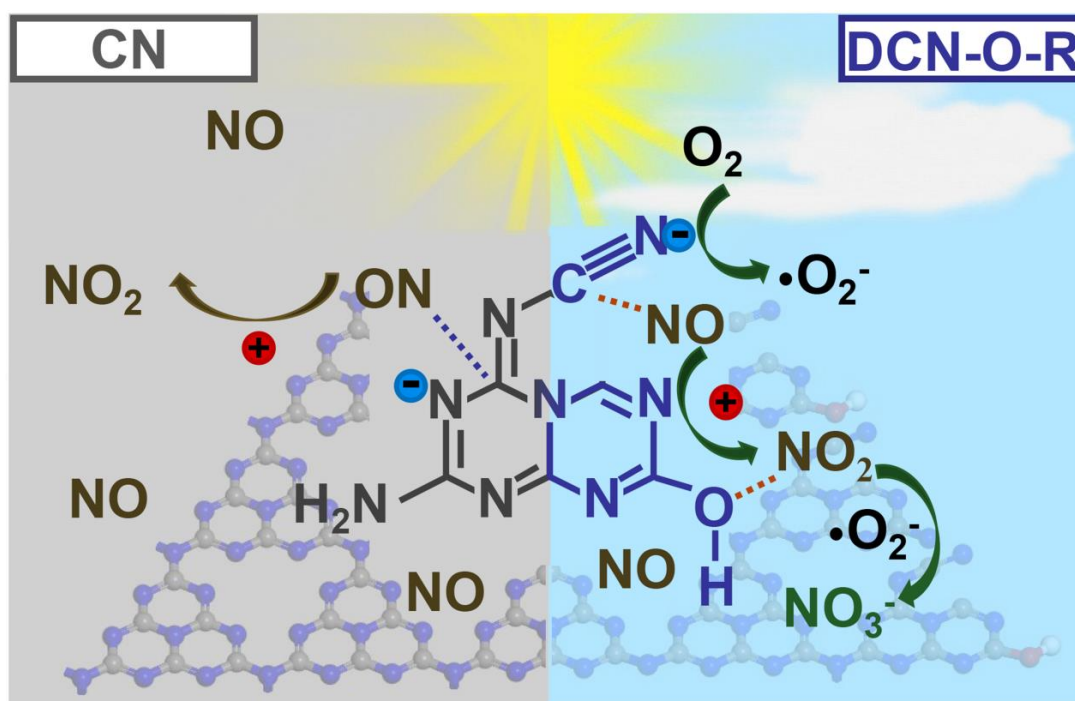


**Figure 10.** Proposed photocatalysis mechanism of NO conversion over CN and DCN-O-R.

### 3. Experimental Section

#### 3.1. Chemical and Reagents

Analytical-grade solvents and reagents were all utilized without additional purification. Ammonium chloride was purchased from Shanghai Macklin Biotechnology Co., Ltd (Shanghai, China), and melamine was purchased from Sigma-Aldrich (St. Louis, MO, USA). During the studies, deionized (DI) water ( $18 \mu S/cm$ ) was utilized.

#### 3.2. Preparation of the Photocatalysts

$g-C_3N_4$  modified with cyano and hydroxyl groups was synthesized using melamine as a precursor and ammonium chloride as the bubbling template. Typically, 1 g of melamine and 6 g of ammonium chloride were finely mixed together in a mortar. The mixture was heated to  $550 \text{ }^\circ\text{C}$  for 4 h in a muffle furnace under air conditioning. The heating rate was  $5 \text{ }^\circ\text{C}\cdot\text{min}^{-1}$ . The product was washed with water in order to remove the salt remnant and dried at  $60 \text{ }^\circ\text{C}$  for 12 h. This sample was denoted as DCN. The pristine  $g-C_3N_4$  was synthesized in the absence of ammonium chloride and denoted as CN.

An amount of 0.6 g of DCN was heated again at  $550 \text{ }^\circ\text{C}$  for 1 h in an uncovered crucible at air to denote DCN-O-R. To obtain a sample of DCN-O-P which benefited from nitrogen vacancies, a similar procedure was repeated in a covered crucible.

### 3.3. Characterization

The crystal phases of the samples were examined by X-ray diffraction (XRD) using Cu K $\alpha$  radiation (model D/max2200PC, Rigaku Co., Tokyo, Japan). The morphology was determined using transmission electron microscopy (TEM, JEM-2010, JEOL Japan Electronics Co., Ltd, Tokyo, Japan). The Autosorb-IQ-MP gas sorption analyzer (ASAP 2460, Micromeritics, Norcross, GA, USA) was utilized to determine the samples' Barret-Joyner-Halenda (BJH) pore size distribution and Brunauer-Emmett-Teller (BET) specific surface area using N<sub>2</sub> as the adsorbate. The BET specific surface area and BJH pore size distribution data can be automatically output by the specific surface area analyzer. According to the BET theory, the single-layer adsorption capacity  $V_m$  can be calculated as  $p/V(p^0 - p) = 1/V_m + (C - 1)/V_m C \cdot p/p^0$ . Then, the specific surface area can be calculated according to the formula:  $S = V_m/22400 \cdot N_A \sigma_m$ . The pore size distribution can be obtained based on the BJH calculation method:  $\ln(p/p^0) = -2\gamma_m/RT\rho \cdot 1/r$ . Utilizing Al K $\alpha$  X-rays ( $h\nu = 1486.6$  eV) at 150 W (AXIS Supra, Kratos, Manchester, UK), X-ray photoelectron spectroscopy (XPS) was used to examine the elemental composition and chemical state of the components. Fourier transform infrared (FT-IR) spectra were obtained using a Bruker (Vertex70, Bruker Corporation, Billerica, MA, USA) spectrophotometer with KBr serving as the reference material. A UV-Vis spectrophotometer (UV-3700, Shimadzu Corporation, Kyoto, Japan) was used to measure the light absorption capacity using UV-Vis diffuse-reflectance spectrometry (UV-Vis DRS) spectra. Using a fluorescence spectrophotometer (LabRAM HR Evolution, Horiba Jobin Yvon, Paris, France) with an excitation wavelength of 420 nm, the photoluminescence (PL) spectra were captured. Using a Bruker ESP 500 spectrometer (Bruker Corporation, Billerica, MA, USA), the electron paramagnetic resonance (EPR) technique was used to identify the nitrogen vacancies and photo-induced reactive oxygen species (ROS) such as  $\bullet\text{OH}$ ,  $\bullet\text{O}_2^-$  and  $^1\text{O}_2$ .

### 3.4. Photocatalytic Performance Tests

As shown in Figure A1, in a continuous flow reactor, the samples' photocatalytic activity was assessed for the elimination of NO at the ppb level using a 300 W Xenon lamp fitted with a 420 nm cut-off filter. To create a homogenous suspension, 50 mg of the sample was first dispersed in 5 mL of 100% ethanol in a Petri dish ( $R = 6$  cm) for 10 min. The solvent was then evaporated by drying the mixture at 60 °C. Finally, the Petri dish was placed within a quartz-covered 0.785 L ( $R = 5$  cm,  $L = 10$  cm) glass reactor. The mixture of NO and air flows continuously into the reactor, and the NO concentration is controlled at about 800 ppb by adjusting the NO flow rate at  $0.284$  L $\cdot$ min<sup>-1</sup>. The O<sub>2</sub> flow rate was set to  $1.29$  L $\cdot$ min<sup>-1</sup> through the mass flow controller. Concentrations of NO and NO<sub>2</sub> were monitored in situ by an NO<sub>x</sub> analyzer (Model 42i, Thermo Fisher Scientific, Waltham, MA, USA). The photocatalytic reaction is initiated by turning on the vertically positioned xenon lamp above the reactor, following the attainment of the adsorption-desorption equilibrium. The efficiency of photocatalytic NO removal was calculated ( $\eta$ ) according to the equation:  $\eta = (1 - C/C_0) \times 100\%$ , where  $C_0$  and  $C$  represent the initial and real-time NO concentrations, respectively.

### 3.5. Active Species Scavenging Experiments

Active species capture experiments were used to elucidate the functions of various radicals and charge carriers in the photocatalytic removal of NO at ambient temperature. The scavenging agents, potassium iodide (KI), potassium dichromate (K<sub>2</sub>Cr<sub>2</sub>O<sub>7</sub>), tert-butanol (TBA), *p*-benzoquinone (PBQ) and histidine (HIS), were added to the system containing the DCN-O-R sample. During the photocatalytic reactions, they functioned to capture the photogenerated holes (h<sup>+</sup>), electrons (e<sup>-</sup>), hydroxyl ( $\bullet\text{OH}$ ), superoxide ( $\bullet\text{O}_2^-$ ) and singlet oxygen ( $^1\text{O}_2$ ) radicals, respectively. The reaction was followed within the same irradiation time of the control experiment to compare the removal efficiencies.

### 3.6. Fluorophotometric Measurements of $H_2O_2$

Place 50 mL of  $H_2O$  and 50 mg of catalyst in a beaker. Stir for 30 min under dark conditions. Take 3 mL of suspension and filter the catalyst. Add 100  $\mu$ L (0.1 g/L) of horseradish enzyme to the liquid, wait for 10 min,  $H_2O_2$  reacts with horseradish enzyme to generate fluorescence signals. Then, add 1 mL of NaOH (0.1 mol) to stop the reaction. Turn on the light and take a sample every 10 min according to the above method. Using fluorescence spectrophotometry for testing, set the excitation wavelength at 409 nm and the emission wavelength at 326 nm.

## 4. Conclusions

Selective photocatalytic conversion of NO was explored over g- $C_3N_4$  co-functionalized with  $-C\equiv N$  and  $-OH$  groups under visible light. DCN-O-R was able to remove NO pollutant twice as efficiently as pristine CN. The production efficiently of the toxic intermediate  $NO_2$  in the presence of DCN-O-R as the photocatalyst was 4.8%, which was significantly lower than that of CN (49%). The mechanistic effects of the functional groups on the photocatalytic NO selective conversion were investigated making use of a combined theoretical–experimental approach. The results indicate that the  $-C\equiv N$  group caused an intermediate energy level in the DCN-O-R sample, thereby ameliorating the light-harvesting properties of the photocatalyst. In addition, the  $-C\equiv N$  groups effectively inhibited the recombination of photogenerated electron–hole pairs and introduced a large amount of effective ROS ( $\bullet O_2^-$ ) into the system. NO adsorbed on the  $-C\equiv N$  sites can be oxidized by  $h^+$  to form a toxic byproduct, ( $NO_2$ ). The  $-OH$  groups promoted further oxidation of  $NO_2$  to  $NO_3^-$ , where  $\bullet O_2^-$  played a major role. The present work not only provides a novel strategy to design efficient photocatalysts towards the heterogeneous selective oxidation of NO, but also provides molecular level insights into the correlation between surface functional groups and photocatalytic pathways to inhibit toxic intermediates.

**Author Contributions:** Conceptualization and Methodology, H.W. and C.W.; Software, H.W.; Validation, H.W.; Data curation, H.W.; Writing—Original draft preparation, H.W.; Visualization and Investigation, H.W., X.X., A.L., S.W., H.R.; Supervision, C.W., Y.H., A.A.A. and A.R.; Writing—Reviewing and Editing, H.W., C.W., M.P. and S.G. All authors have read and agreed to the published version of the manuscript.

**Funding:** This research was funded by the National Natural Science Foundation of China (Nos. 52161145409, 21976116), Iranian National Science Foundation (Grant No. 4001153), and Researchers Supporting Project number (RSPD2023R691), King Saud University, Riyadh, Saudi Arabia.

**Data Availability Statement:** Data is contained within the article.

**Conflicts of Interest:** The authors declare no conflict of interest.

## Appendix A

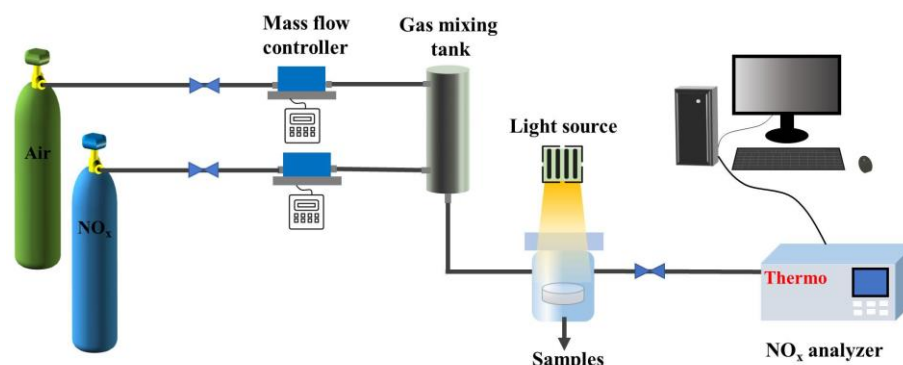


**Figure A1.** The reaction device diagram.

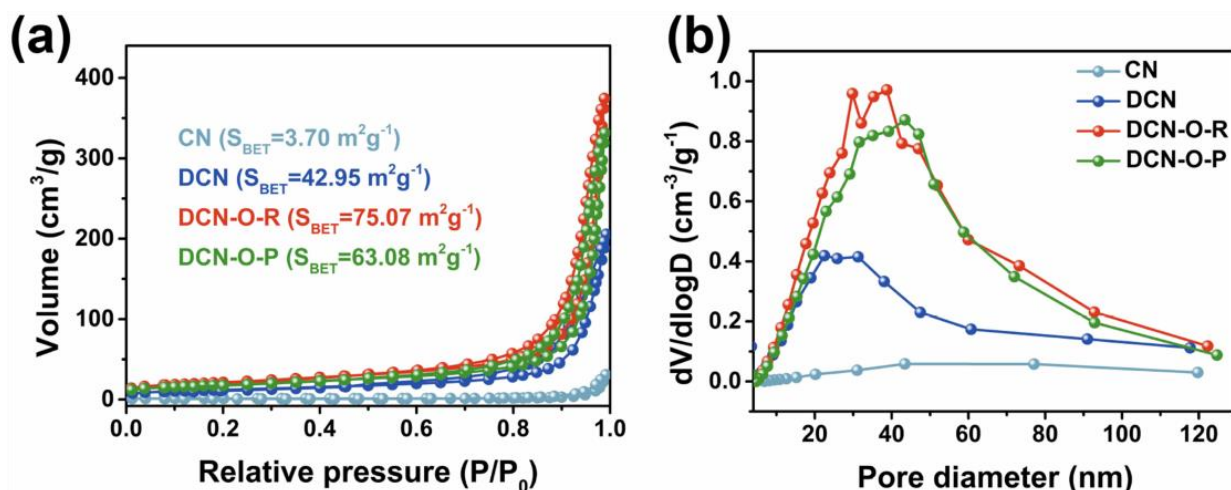


Figure A2. (a) Nitrogen adsorption-desorption isotherms; and (b) BJH pore size distribution of CN, DCN and DCN-x samples.

Table A1. Table with the ratios of N-to-C and O-to-C in all four catalysts.

Photocatalysts	N/C	O/C
CN	1.190	0.053
DCN	1.176	0.053
DCNO-P	1.173	0.063
DCNO-R	1.049	0.069

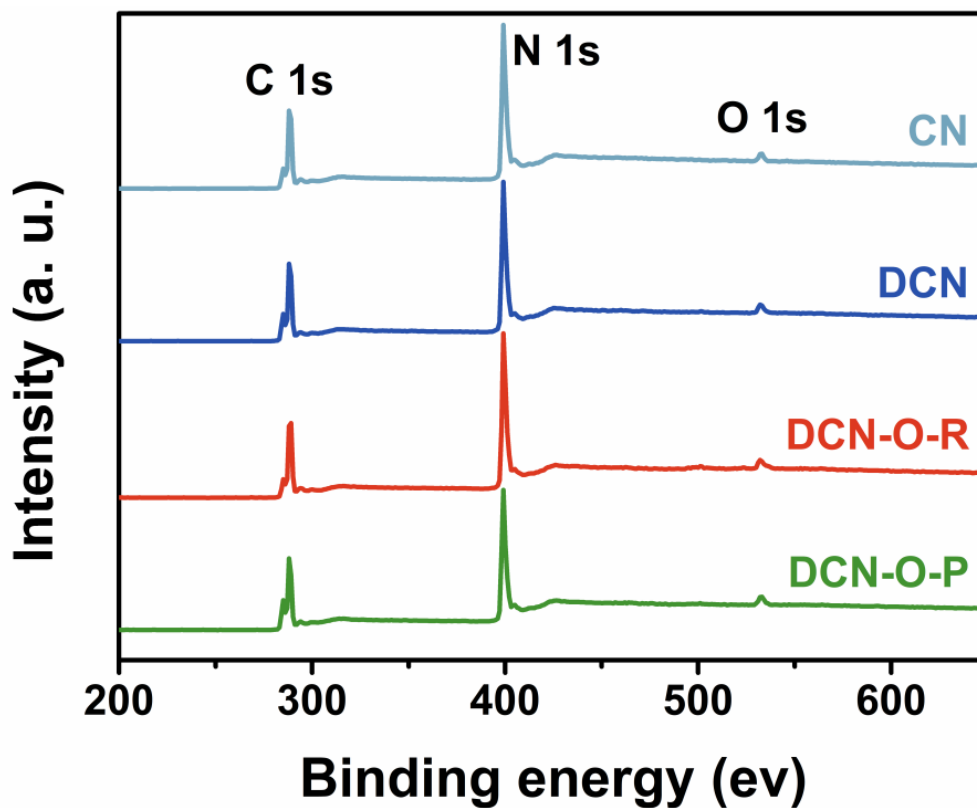


Figure A3. XPS Survey spectrum of CN, DCN, and DCN-x samples.

## References

1. Huang, Y.; Liang, Y.L.; Rao, Y.F.; Zhu, D.D.; Cao, J.-J.; Shen, Z.; Ho, W.K.; Lee, C.S. Environment-Friendly Carbon Quantum Dots/ZnFe<sub>2</sub>O<sub>4</sub> Photocatalysts: Characterization, Biocompatibility, and Mechanisms for NO Removal. *Environ. Sci. Technol.* **2017**, *51*, 2924–2933. [[CrossRef](#)] [[PubMed](#)]
2. Kreuzer, L.B.; Patel, C.K. Nitric Oxide Air Pollution: Detection by Optoacoustic Spectroscopy. *Science* **1971**, *173*, 45–47. [[CrossRef](#)] [[PubMed](#)]
3. Han, X.; Yang, S.H.; Schroder, M. Porous Metal-organic Frameworks as Emerging Sorbents for Clean Air. *Nat. Rev. Chem.* **2019**, *3*, 108–118. [[CrossRef](#)]
4. Yu, J.J.; Jiang, Z.; Zhu, L.; Hao, Z.P.; Xu, Z.P. Adsorption/desorption Studies of NO<sub>x</sub> on Well-mixed Oxides Derived from Co-Mg/Al Hydrotalcite-like Compounds. *J. Phys. Chem. B* **2006**, *110*, 4291–4300. [[CrossRef](#)]
5. Rodriguez, J.A.; Jirsak, T.; Liu, G.; Hrbek, J.; Dvorak, J.; Maiti, A. Chemistry of NO<sub>2</sub> on Oxide Surfaces: Formation of NO<sub>3</sub> on TiO<sub>2</sub> (110) and NO<sub>2</sub> ↔ O Vacancy Interactions. *J. Am. Chem. Soc.* **2001**, *123*, 9597–9605. [[CrossRef](#)] [[PubMed](#)]
6. Dong, F.; Zhao, Z.W.; Sun, Y.J.; Zhang, Y.X.; Yan, S.; Wu, Z.B. An Advanced Semimetal-Organic Bi Spheres-g-C<sub>3</sub>N<sub>4</sub> Nanohybrid with SPR-Enhanced Visible-Light Photocatalytic Performance for NO Purification. *Environ. Sci. Technol.* **2015**, *49*, 12432–12440. [[CrossRef](#)]
7. Zhu, H.Z.; Nie, Z.G.; Hu, Y.F.; Wang, J.Y.; Bai, H.; Li, Y.; Guo, Q.J.; Wang, C.P. Experimental Study on Denitration Performance of Iron Complex-Based Absorption Solutions and Their Regeneration by Zn. *Energy Fuels* **2019**, *33*, 8998–9003. [[CrossRef](#)]
8. Klose, W.; Rincon, S. Adsorption and Reaction of NO on Activated Carbon in the Presence of Oxygen and Water Vapour. *Fuel* **2007**, *86*, 203–209. [[CrossRef](#)]
9. Lee, J.; Theis, J.R.; Kyriakidou, E.A. Vehicle Emissions Trapping Materials: Successes, Challenges, and the Path Forward. *Appl. Catal. B-Environ.* **2019**, *243*, 397–414. [[CrossRef](#)]
10. Wang, X.Q.; Liu, Y.; Wu, Z.B. The Poisoning Mechanisms of Different Zinc Species on a Ceria-based NH<sub>3</sub>-SCR Catalyst and the Co-effects of Zinc and Gas-phase Sulfur/chlorine Species. *J. Colloid. Interf. Sci.* **2020**, *566*, 153–162. [[CrossRef](#)]
11. Seneque, M.; Can, F.; Duprez, D.; Courtois, X. NO<sub>x</sub> Selective Catalytic Reduction (NO<sub>x</sub>-SCR) by Urea: Evidence of the Reactivity of HNCO, Including a Specific Reaction Pathway for NO<sub>x</sub> Reduction Involving NO + NO<sub>2</sub>. *ACS Catal.* **2016**, *6*, 4064–4067. [[CrossRef](#)]
12. Ma, L.; Li, J.H.; Ke, R.; Fu, L.X. Catalytic Performance, Characterization, and Mechanism Study of Fe<sub>2</sub>(SO<sub>4</sub>)<sub>3</sub>/TiO<sub>2</sub> Catalyst for Selective Catalytic Reduction of NO<sub>x</sub> by Ammonia. *J. Phys. Chem. C* **2011**, *115*, 7603–7612. [[CrossRef](#)]
13. Fu, S.L.; Song, Q.; Yao, Q. Mechanism Study on the Adsorption and Reactions of NH<sub>3</sub>, NO, and O<sub>2</sub> on the CaO Surface in the SNCR deNO<sub>x</sub> Process. *Chem. Eng. J.* **2016**, *285*, 137–143. [[CrossRef](#)]
14. Zhou, M.; Dong, G.H.; Yu, F.K.; Huang, Y. The Deep Oxidation of NO Was Realized by Sr multi-site Doped g-C<sub>3</sub>N<sub>4</sub> Via Photocatalytic Method. *Appl. Catal. B-Environ.* **2019**, *256*, 117825. [[CrossRef](#)]
15. Ai, Z.H.; Ho, W.K.; Lee, S.C.; Zhang, L.Z. Efficient Photocatalytic Removal of NO in Indoor Air with Hierarchical Bismuth Oxybromide Nanoplate Microspheres under Visible Light. *Environ. Sci. Technol.* **2009**, *43*, 4143–4150. [[CrossRef](#)] [[PubMed](#)]
16. Dong, G.H.; Jacobs, D.L.; Zang, L.; Wang, C.Y. Carbon Vacancy Regulated Photoreduction of NO to N<sub>2</sub> Over Ultrathin g-C<sub>3</sub>N<sub>4</sub> Nanosheets. *Appl. Catal. B-Environ.* **2017**, *218*, 515–524. [[CrossRef](#)]
17. Wang, X.C.; Maeda, K.; Thomas, A.; Takanabe, K.; Xin, G.; Carlsson, J.M.; Domen, K.; Antonietti, M. A Metal-free Polymeric Photocatalyst for Hydrogen Production from Water under Visible Light. *Nat. Mater.* **2009**, *8*, 76–80. [[CrossRef](#)]
18. Choi, C.H.; Lin, L.; Gim, S.; Lee, S.; Kim, H.; Wang, X.; Choi, W. Polymeric Carbon Nitride with Localized Aluminum Coordination Sites as a Durable and Efficient Photocatalyst for Visible Light Utilization. *ACS Catal.* **2018**, *8*, 4241–4256. [[CrossRef](#)]
19. Dong, F.; Zhao, Z.W.; Xiong, T.; Ni, Z.L.; Zhang, W.; Sun, Y.J.; Ho, W.K. In Situ Construction of g-C<sub>3</sub>N<sub>4</sub>/g-C<sub>3</sub>N<sub>4</sub> Metal-Free Heterojunction for Enhanced Visible-Light Photocatalysis. *ACS Appl. Mater. Interfaces* **2013**, *5*, 11392–11401. [[CrossRef](#)]
20. Moon, G.H.; Fujitsuka, M.; Kim, S.; Majima, T.; Wang, X.; Choi, W. Eco-Friendly Photochemical Production of H<sub>2</sub>O<sub>2</sub> through O<sub>2</sub> Reduction over Carbon Nitride Frameworks Incorporated with Multiple Heteroelements. *ACS Catal.* **2017**, *7*, 2886–2895. [[CrossRef](#)]
21. Dong, G.H.; Zhao, L.L.; Wu, X.X.; Zhu, M.S.; Wang, F. Photocatalysis Removing of NO Based on Modified Carbon Nitride: The Effect of Celestite Mineral Particles. *Appl. Catal. B-Environ.* **2019**, *245*, 459–468. [[CrossRef](#)]
22. Luo, J.M.; Dong, G.H.; Zhu, Y.Q.; Yang, Z.; Wang, C.Y. Switching of Semiconducting Behavior from n-type to p-type Induced High Photocatalytic NO Removal Activity in g-C<sub>3</sub>N<sub>4</sub>. *Appl. Catal. B-Environ.* **2017**, *214*, 46–56. [[CrossRef](#)]
23. Dong, X.A.; Li, J.Y.; Xing, Q.; Zhou, Y.; Huang, H.W.; Dong, F. The Activation of Reactants and Intermediates Promotes the Selective Photocatalytic NO Conversion on Electron-localized Sr-intercalated g-C<sub>3</sub>N<sub>4</sub>. *Appl. Catal. B-Environ.* **2018**, *232*, 69–76. [[CrossRef](#)]
24. Huang, H.W.; Xiao, K.; Tian, N.; Dong, F.; Zhang, T.; Du, X.; Zhang, Y.H. Template-free Precursor-surface-etching Route to Porous, Thin g-C<sub>3</sub>N<sub>4</sub> Nanosheets for Enhancing Photocatalytic Reduction and Oxidation Activity. *J. Mater. Chem. A* **2017**, *5*, 17452–17463. [[CrossRef](#)]
25. Xiong, T.; Cen, W.L.; Zhang, Y.X.; Dong, F. Bridging the g-C<sub>3</sub>N<sub>4</sub> Interlayers for Enhanced Photocatalysis. *ACS Catal.* **2016**, *6*, 2462–2472. [[CrossRef](#)]
26. Ran, M.X.; Li, J.R.; Cui, W.; Li, Y.H.; Li, P.D.; Dong, F. Efficient and Stable Photocatalytic NO Removal on C Self-doped g-C<sub>3</sub>N<sub>4</sub>: Electronic Structure and Reaction Mechanism. *Catal. Sci. Technol.* **2018**, *8*, 3387–3394. [[CrossRef](#)]



27. Liao, J.Z.; Cui, W.; Li, J.Y.; Sheng, J.P.; Wang, Z.M.; Dong, X.; Chen, P.; Jiang, G.; Wang, Z.; Dong, F. Nitrogen Defect Structure and NO Plus Intermediate Promoted Photocatalytic NO Removal on H<sub>2</sub> Treated g-C<sub>3</sub>N<sub>4</sub>. *Chem. Eng. J.* **2020**, *379*, 122282. [[CrossRef](#)]
28. Wang, J.D.; Cui, W.; Chen, R.M.; He, Y.; Yuan, C.; Sheng, J.; Li, J.; Zhang, Y.; Dong, F.; Sun, Y. OH/Na Co-functionalized Carbon Nitride: Directional Charge Transfer and Enhanced Photocatalytic Oxidation Ability. *Catal. Sci. Technol.* **2020**, *10*, 529–535. [[CrossRef](#)]
29. Liu, G.M.; Huang, Y.; Lv, H.Q.; Wang, H.; Zeng, Y.; Yuan, M.; Meng, Q.G.; Wang, C.Y. Confining Single-atom Pd on g-C<sub>3</sub>N<sub>4</sub> with Carbon Vacancies Towards Enhanced Photocatalytic NO Conversion. *Appl. Catal. B-Environ.* **2021**, *284*, 119683. [[CrossRef](#)]
30. Fan, J.H.; Qin, H.H.; Jiang, S.M. Mn-doped g-C<sub>3</sub>N<sub>4</sub> Composite to Activate Peroxymonosulfate for Acetaminophen Degradation: The Role of Superoxide Anion and Singlet Oxygen. *Chem. Eng. J.* **2019**, *359*, 723–732. [[CrossRef](#)]
31. Geng, Y.X.; Chen, D.Y.; Li, N.J.; Xu, Q.F.; Li, H.; He, J.; Lu, J.M. Z-Scheme 2D/2D Alpha-Fe<sub>2</sub>O<sub>3</sub>/g-C<sub>3</sub>N<sub>4</sub> Heterojunction for Photocatalytic Oxidation of Nitric Oxide. *Appl. Catal. B-Environ.* **2021**, *280*, 119409. [[CrossRef](#)]
32. Yang, J.; Liang, Y.J.; Li, K.; Yang, G.; Wang, K.; Xu, R.; Xie, X.J. One-step Synthesis of Novel K<sup>+</sup> and Cyano Groups Decorated Triazine-/heptazine-based g-C<sub>3</sub>N<sub>4</sub> Tubular Homojunctions for Boosting Photocatalytic H<sub>2</sub> Evolution. *Appl. Catal. B-Environ.* **2020**, *262*, 118252. [[CrossRef](#)]
33. Shi, Y.H.; Li, J.S.; Wan, D.J.; Huang, J.H.; Liu, Y.D. Peroxymonosulfate-enhanced Photocatalysis by Carbonyl-modified g-C<sub>3</sub>N<sub>4</sub> for Effective Degradation of the Tetracycline Hydrochloride. *Sci. Total Environ.* **2020**, *749*, 142313. [[CrossRef](#)] [[PubMed](#)]
34. Bai, J.Y.; Wang, L.J.; Zhang, Y.J.; Wen, C.F.; Wang, X.L.; Yang, H.G. Carboxyl Functionalized Graphite Carbon Nitride for Remarkably Enhanced Photocatalytic Hydrogen Evolution. *Appl. Catal. B-Environ.* **2020**, *266*, 118590. [[CrossRef](#)]
35. Zhang, S.; Song, S.; Gu, P.C.; Ma, R.; Wei, D.; Zhao, G.; Wen, T.; Jehan, R.; Hu, B.W.; Wang, X.K. Visible-light-driven Activation of Persulfate Over Cyano and Hydroxyl Group Co-modified Mesoporous g-C<sub>3</sub>N<sub>4</sub> for Boosting Bisphenol A Degradation. *J. Mater. Chem. A* **2019**, *7*, 5552–5560. [[CrossRef](#)]
36. Zeng, Q.M.; Ni, J.P.; Mariotti, D.; Lu, L.Y.; Chen, H.; Ni, C.S. Plasma-treatment of Polymeric Carbon Nitride for Efficient NO Abatement under Visible Light. *J. Phys. D Appl. Phys.* **2022**, *55*, 354003. [[CrossRef](#)]
37. Xiao, Y.T.; Tian, G.H.; Li, W.; Xie, Y.; Jiang, B.; Tian, C.; Zhao, D.Y.; Fu, H.G. Molecule Self-Assembly Synthesis of Porous Few-Layer Carbon Nitride for Highly Efficient Photoredox Catalysis. *J. Am. Chem. Soc.* **2019**, *141*, 2508–2515. [[CrossRef](#)]
38. Huang, Z.H.; Chen, H.; Zhao, L.; Fang, W.; He, X.; Li, W.X.; Tian, P. In Suit Inducing Electron-donating and Electron-withdrawing Groups in Carbon Nitride by One-step NH<sub>4</sub>Cl-assisted Route: A Strategy for High Solar Hydrogen Production Efficiency. *Environ. Int.* **2019**, *126*, 289–297. [[CrossRef](#)]
39. She, X.J.; Liu, L.; Ji, H.Y.; Mo, Z.; Li, Y.; Huang, L.; Du, D.; Xu, H.; Li, H.M. Template-free Synthesis of 2D Porous Ultrathin Nonmetal-doped g-C<sub>3</sub>N<sub>4</sub> Nanosheets with Highly Efficient Photocatalytic H<sub>2</sub> Evolution from Water under Visible Light. *Appl. Catal. B-Environ.* **2016**, *187*, 144–153. [[CrossRef](#)]
40. Dong, G.H.; Ho, W.K.; Wang, C.Y. Selective Photocatalytic N<sub>2</sub> Fixation Dependent on g-C<sub>3</sub>N<sub>4</sub> Induced by Nitrogen Vacancies. *J. Mater. Chem. A* **2015**, *3*, 23435–23441. [[CrossRef](#)]
41. Zhang, D.; Guo, Y.L.; Zhao, Z.K. Porous Defect-modified Graphitic Carbon Nitride via a Facile One-step Approach with Significantly Enhanced Photocatalytic Hydrogen Evolution under Visible Light Irradiation. *Appl. Catal. B-Environ.* **2018**, *226*, 1–9. [[CrossRef](#)]
42. Song, X.P.; Yang, Q.; Jiang, X.H.; Yin, M.Y.; Zhou, L.M. Porous Graphitic Carbon Nitride Nanosheets Prepared under Self-producing Atmosphere for Highly Improved Photocatalytic Activity. *Appl. Catal. B-Environ.* **2017**, *217*, 322–330. [[CrossRef](#)]
43. He, F.; Chen, G.; Yu, Y.G.; Zhou, Y.S.; Zheng, Y.; Hao, S. The Sulfur-bubble Template-mediated Synthesis of Uniform Porous g-C<sub>3</sub>N<sub>4</sub> with Superior Photocatalytic Performance. *Chem. Commun.* **2015**, *51*, 425–427. [[CrossRef](#)] [[PubMed](#)]
44. Guo, F.; Shi, W.L.; Zhu, C.; Li, H.; Kang, Z.H. CoO and g-C<sub>3</sub>N<sub>4</sub> Complement Each Other for Highly Efficient Overall Water Splitting under Visible Light. *Appl. Catal. B-Environ.* **2018**, *226*, 412–420. [[CrossRef](#)]
45. Guo, F.; Shi, W.L.; Wang, H.B.; Huang, H.; Liu, Y.; Kang, Z.H. Fabrication of a CuBi<sub>2</sub>O<sub>4</sub>/g-C<sub>3</sub>N<sub>4</sub> p-n Heterojunction with Enhanced Visible Light Photocatalytic Efficiency Toward Tetracycline Degradation. *Inorg. Chem. Front.* **2017**, *4*, 1714–1720. [[CrossRef](#)]
46. Yang, S.B.; Gong, Y.J.; Zhang, J.S.; Zhan, L.; Ma, L.; Fang, Z.; Vajtai, R.; Wang, X.C.; Ajayan, P.M. Exfoliated Graphitic Carbon Nitride Nanosheets as Efficient Catalysts for Hydrogen Evolution Under Visible Light. *Adv. Mater.* **2013**, *25*, 2452–2456. [[CrossRef](#)]
47. Yang, J.; Liang, Y.J.; Li, K.; Yang, G.; Wang, K.; Xu, R.; Xie, X.J. Cyano and Potassium-rich g-C<sub>3</sub>N<sub>4</sub> Hollow Tubes for Efficient Visible-light-driven Hydrogen Evolution. *Catal. Sci. Technol.* **2019**, *9*, 3342–3346. [[CrossRef](#)]
48. Che, H.N.; Liu, L.H.; Che, G.B.; Dong, H.J.; Liu, C.B.; Li, C.M. Control of Energy Band, Layer Structure and Vacancy Defect of Graphitic Carbon Nitride by Intercalated Hydrogen Bond Effect of NO<sub>3</sub><sup>-</sup> Toward Improving Photocatalytic Performance. *Chem. Eng. J.* **2019**, *357*, 209–219. [[CrossRef](#)]
49. Gu, Z.Y.; Cui, Z.T.; Wang, Z.J.; Qin, K.S.; Asakura, Y.; Hasegawa, T.; Tsukuda, S.; Hongo, K.; Maezono, R.; Yin, S. Carbon Vacancies and Hydroxyls in Graphitic Carbon Nitride: Promoted Photocatalytic NO Removal Activity and Mechanism. *Appl. Catal. B-Environ.* **2020**, *279*, 119376. [[CrossRef](#)]
50. Ho, W.K.; Zhang, Z.Z.; Xu, M.K.; Zhang, X.W.; Wang, X.X.; Huang, Y. Enhanced Visible-light-driven Photocatalytic Removal of NO: Effect on Layer Distortion on g-C<sub>3</sub>N<sub>4</sub> by H<sub>2</sub> Heating. *Appl. Catal. B-Environ.* **2015**, *179*, 106–112. [[CrossRef](#)]
51. Liang, Q.H.; Li, Z.; Yu, X.L.; Huang, Z.H.; Kang, F.Y.; Yang, Q.H. Macroscopic 3D Porous Graphitic Carbon Nitride Monolith for Enhanced Photocatalytic Hydrogen Evolution. *Adv. Mater.* **2015**, *27*, 4634–4639. [[CrossRef](#)] [[PubMed](#)]

52. Yang, P.J.; Wang, L.; Zhuzhang, H.Y.; Wang, R.R.; Titirici, M.M.; Wang, X.C. Photocarving Nitrogen Vacancies in a Polymeric Carbon Nitride for Metal-free Oxygen Synthesis. *Appl. Catal. B-Environ.* **2019**, *256*, 117794. [[CrossRef](#)]
53. Tang, J.L.; Liu, Y.S.; Hu, Y.J.; Huang, J.W.; Wang, B.; Yang, C.T.; Yang, G.C. Ultrafast NaN<sub>3</sub>-deflagration Induced Nitrogen Vacancy-enriched g-C<sub>3</sub>N<sub>4</sub> for Tailoring Band Structures and Enhanced Photocatalytic Performance. *J. Power Sources* **2019**, *434*, 226731. [[CrossRef](#)]
54. Ma, W.; Wang, N.; Guo, Y.; Yang, L.Q.; Lv, M.; Tang, X.; Li, S.T. Enhanced Photoreduction CO<sub>2</sub> Activity on g-C<sub>3</sub>N<sub>4</sub>: By Synergistic Effect of Nitrogen Defective-enriched and Porous Structure, and Mechanism Insights. *Chem. Eng. J.* **2020**, *388*, 124288. [[CrossRef](#)]
55. Cao, J.W.; Zhang, J.Y.; Dong, X.A.; Fu, H.L.; Zhang, X.; Lv, X.; Li, Y.H.; Jiang, G.M. Defective Borate-decorated Polymer Carbon Nitride: Enhanced Photocatalytic NO Removal, Synergy Effect and Reaction Pathway. *Appl. Catal. B-Environ.* **2019**, *249*, 266–274. [[CrossRef](#)]
56. Ren, H.T.; Qi, F.; Labidi, A.; Zhao, J.J.; Wang, H.; Xin, Y.; Luo, J.M.; Wang, C.Y. Chemically bonded carbon quantum dots/Bi<sub>2</sub>WO<sub>6</sub> S-scheme heterojunction for boosted photocatalytic antibiotic degradation: Interfacial engineering and mechanism insight. *Appl. Catal. B-Environ.* **2023**, *330*, 122587. [[CrossRef](#)]
57. Wang, C.; Fu, M.; Cao, J.; Wu, X.L.; Hu, X.L.; Dong, F. BaWO<sub>4</sub>/g-C<sub>3</sub>N<sub>4</sub> Heterostructure with Excellent Bifunctional Photocatalytic Performance. *Chem. Eng. J.* **2020**, *385*, 123833. [[CrossRef](#)]
58. Tan, Y.W.; Wei, S.P.; Liu, X.Y.; Pan, B.Y.; Liu, S.; Wu, J.; Fu, M.; Jia, Y.M.; He, Y.Z. Neodymium oxide (Nd<sub>2</sub>O<sub>3</sub>) coupled tubular g-C<sub>3</sub>N<sub>4</sub>, an efficient dual-function catalyst for photocatalytic hydrogen production and NO removal. *Sci. Total Environ.* **2021**, *773*, 145583. [[CrossRef](#)]
59. Li, J.L.; Zhang, Q.; Zou, Y.Z.; Cao, Y.H.; Cui, W.; Dong, F.; Zhou, Y. Ti<sub>3</sub>C<sub>2</sub> MXene modified g-C<sub>3</sub>N<sub>4</sub> with enhanced visible-light photocatalytic performance for NO purification. *J. Colloid. Interf. Sci.* **2020**, *575*, 443–451. [[CrossRef](#)]
60. Ren, Y.Y.; Li, Y.; Wu, X.Y.; Wang, J.L.; Zhang, G.K. S-scheme Sb<sub>2</sub>WO<sub>6</sub>/g-C<sub>3</sub>N<sub>4</sub> Photocatalysts with Enhanced Visible-light-induced Photocatalytic NO Oxidation Performance. *Chin. J. Catal.* **2021**, *42*, 69–77. [[CrossRef](#)]
61. Cui, W.; Li, J.Y.; Dong, F.; Sun, Y.J.; Jiang, G.; Cen, W.; Lee, S.C.; Wu, Z.B. Highly Efficient Performance and Conversion Pathway of Photocatalytic NO Oxidation on SrO-Clusters@Amorphous Carbon Nitride. *Environ. Sci. Technol.* **2017**, *51*, 10682–10690. [[CrossRef](#)] [[PubMed](#)]
62. Ruan, H.D.; Frost, R.L.; Klopogge, J.T.; Duong, L. Infrared spectroscopy of goethite dehydroxylation: III. FT-IR microscopy of in situ study of the thermal transformation of goethite to hematite. *Spectrochim. Acta A.* **2002**, *58*, 443–451. [[CrossRef](#)] [[PubMed](#)]

**Disclaimer/Publisher's Note:** The statements, opinions and data contained in all publications are solely those of the individual author(s) and contributor(s) and not of MDPI and/or the editor(s). MDPI and/or the editor(s) disclaim responsibility for any injury to people or property resulting from any ideas, methods, instructions or products referred to in the content.